# Temperature dependence of the upper critical field of FeSe single crystals

S. I. Vedeneev,[1,2] B. A. Piot,[1] D. K. Maude,[1] and A. V. Sadakov[2]

[1]*Laboratoire National des Champs Magnétiques Intenses, CNRS-UJF-UPS-INSA, 25 avenue des Martyrs, 38042 Grenoble, France*

[2]*P.N. Lebedev Physical Institute, Russian Academy of Sciences, 119991 Moscow, Russia*

(Received 22 December 2012; revised manuscript received 2 March 2013; published 18 April 2013)

We present a careful study of the resistive superconducting transition in FeSe single crystals down to $T = 40$ mK in continuous magnetic fields up to 30 T applied perpendicular and parallel to the $ab$ plane. In the **H**$\|$**c** geometry the temperature dependence of the resistive upper critical field $H_{c2}^{*}$, determined as the field at which the in-plane resistivity in the transition region is 90% of the normal state resistivity is down to temperatures $T/T_c < 0.006$, is in close agreement with the Werthamer-Helfand-Hohenberg (WHH) theoretical curve which describes the behavior of the upper critical field in conventional type-II superconductors. In contrast, for the **H**$\|$**ab** geometry, the data depart from the WHH model with increasing applied magnetic field according to the paramagnetic limitation of superconductivity. An anisotropy parameter $\gamma$ in our FeSe crystals decreases with decreasing temperature and FeSe becomes nearly isotropic when the temperature $T \to 0$.

DOI: 10.1103/PhysRevB.87.134512 PACS number(s): 74.62.Bf, 74.10.+v, 74.20.Mn, 74.70.Dd

## I. INTRODUCTION

In 2008, Hsu *et al.*[1] reported on the observation of superconductivity with $T_c \sim 8$ K in the tetragonal phase of the layered iron chalcogenide FeSe ($\beta$-FeSe). Subsequent work has revealed resistivity onsets for the superconducting transition at temperatures as high as 13.5 K at ambient pressure.[2] The highest transition temperatures in this high-temperature superconductor[3] are found when the compound is closest to stoichiometric, with formula $Fe_{1.01}Se$.[4] The interest in the binary superconductor FeSe is caused by the relative structural simplicity among the Fe-based superconductors, and a number of researchers take FeSe as a model system to study the mechanism of superconductivity in Fe pnictides and chalcogenides.[4–7] At the same time, despite the fact that the upper critical field $H_{c2}(0)$ is one of the fundamental parameters for superconductivity, and despite intense experimental investigation, some ambiguity remains concerning the value, and the temperature dependence, of $H_{c2}$ in iron-based superconductors. In addition, a possible Pauli limitation of the upper critical field is currently debated in the literature.[8–10] Due to the low $T_c$, FeSe is an excellent choice to investigate the superconducting and normal state transport properties in the $T \to 0$ limit. In this paper we present a careful study of the resistive superconducting transition in the iron chalcogenide FeSe over a wide range of temperature down to 40 mK. We describe in addition an experimental study of the temperature dependence of the resistive upper critical field $H_{c2}^{*}$ in FeSe crystals. The magnetotransport measurements were performed in *dc* magnetic fields up to 9 T in a Quantum Design physical property measurement system (PPMS-9) from 1.8 to 20 K and in a 30-T-resistive magnet at the National High Magnetic Field Laboratory in Grenoble. We note that measurements of the upper critical fields $H_{c2}(T)$ in FeSe single crystals at temperatures down to 0.35 K in a static magnet up to 35 T were performed very recently by Lei *et al.*[11] Unlike our experiments, the $H_{c2}$ was determined by measuring the magnetic field dependence of radio-frequency penetration depth. Moreover, in Ref. 11 the normal direction of FeSe crystal plane was (101) rather than (001) for our samples grown at low temperatures, making the two investigations fundamentally different.

## II. EXPERIMENT

The investigated crystals $FeSe_x$ were grown by a KCl-solution-melt free growth method.[12] The crystals have a plateletlike shape and mirrorlike surfaces with typical dimensions (2.5–3) mm × (1.5–2) mm × (50–60) $\mu$m. The quality of the crystals was systematically verified by measurements of the *dc* resistance, *ac* susceptibility, x-ray diffraction, and scanning electron microscopy. The actual cationic composition of the samples used was measured at 20–60 different points on the crystal with a step of 100–200 $\mu$m, and the scatter in the data was less than 2%. The average elemental composition corresponds to the formula $FeSe_{0.89-0.90}$. The x-ray diffraction analysis showed the coexistence of the tetragonal and hexagonal FeSe phases in a variable composition. The phases have the lattice parameters $a = 3.780$ Å, $c = 5.490$ Å and $a = 3.605$ Å, $c = 5.889$ Å for the tetragonal and hexagonal phases, respectively.

Figure 1 in the upper part shows scanning electron micrographs of as-grown $FeSe_{0.9}$ crystals with different shapes where the composition measurement points are denoted by crosses. X-ray diffraction pattern (a) shows the (001) and (004) peaks of the tetragonal (T), plus three peaks of the hexagonal (H) FeSe phase. X-ray diffraction pattern (b) has only the (00N) peaks of the tetragonal phase suggesting that the crystallographic $c$ axis is perpendicular to the plane of the platelike crystals.

A four-probe contact configuration, with symmetrical positions of the low-resistance contacts ($< 1\Omega$) on both $ab$ surfaces of the sample was used for the measurements of $R_{ab}$ and $R_c$ resistances. The temperature and magnetic field dependence of the resistances $R_{ab}(T,H)$ and $R_c(T,H)$ were measured using a lock-in amplifier driven at ≈10.7 Hz. The *ac* current applied was 50 $\mu$A for in-plane and 0.5 mA for out-of-plane resistance measurements. The transport current was in the $ab$ plane of the crystals and orthogonal to the field. A $RuO_2$ thermometer was used to measure the local temperature of the sample. The field sweep rate $dH/dt = 0.5$ T/min at temperatures 30–150 mK and 1 T/min at higher temperatures was chosen in order to avoid eddy current heating. The temperature was continuously recorded during each measurement sweep. The

 

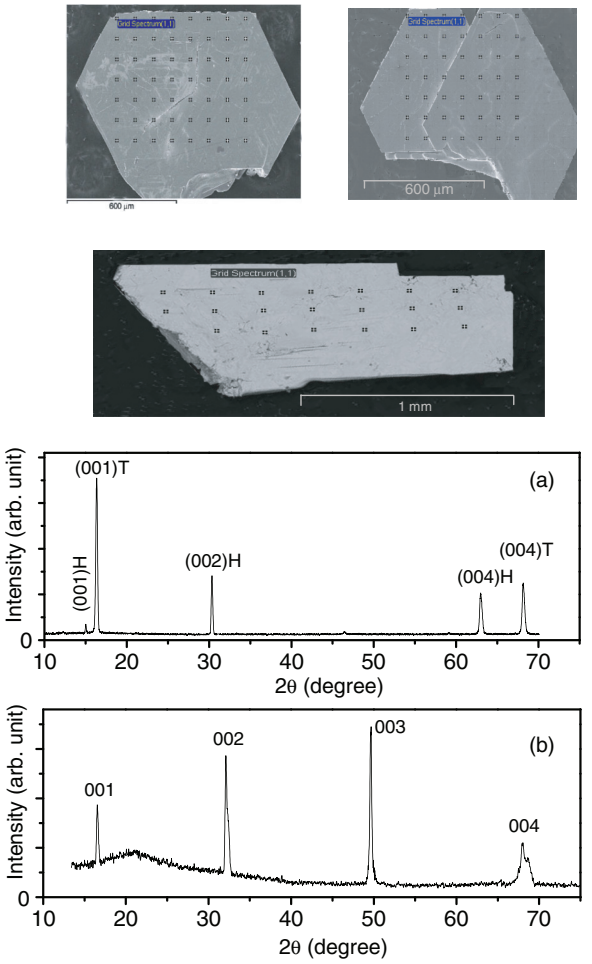


FIG. 1. (Color online) Top: scanning electron micrographs of as-grown $FeSe_{0.9}$ crystals with different shapes where the composition measurement points are denoted by crosses. Bottom: (a) x-ray diffraction pattern showing the peaks of the tetragonal (T), and hexagonal (H) FeSe phases. X-ray diffraction pattern (b) shows only the (00N) peaks of the tetragonal phase.

measured resistances were then converted to the respective resistivities $\rho_{ab}$ and $\rho_c$ using the crystal dimensions which were measured with a high resolution optical microscope. For the low temperature magnetotransport measurements, the crystals were placed directly inside the mixing chamber of a Kelvinox top-loading dilution refrigerator. The crystals were studied with the magnetic field **H** applied either parallel or perpendicular to the $c$ axis. In the latter case a configuration with the in-plane transport current **J** perpendicular to **H** was used. To summarize the properties of the investigated crystals, we have regrouped in Table I the data of tetragonal phase percent $T_c$, slopes $(dH^*_{c2\|c}/dT)_{T_c'}$ and $(dH^*_{c2\|ab}/dT)_{T_c'}$, upper critical fields $H^*_{c2\|c}(0)$ and $H^*_{c2\|ab}(0)$, coherence lengths at zero temperature $\xi_{ab}$ and $\xi_c$.

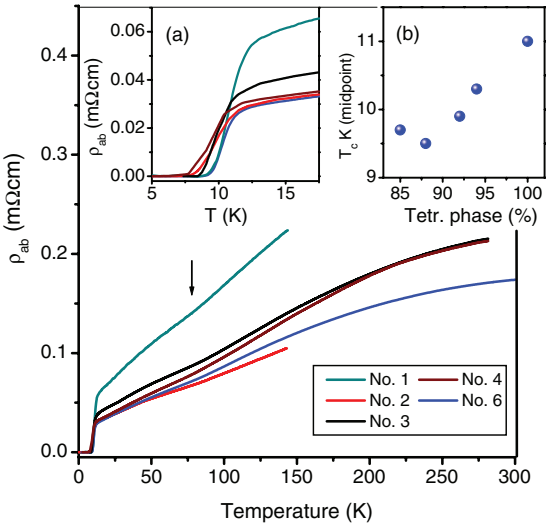


FIG. 2. (Color online) Temperature dependence of the in-plane resistivity ($\rho_{ab}$) as a function of temperature for FeSe samples with different tetragonal phase concentrations. The arrow indicates the tetragonal-to-orthorhombic structural transition. The inset (a) shows an enlarged view of the resistivity near $T_c$. The inset (b) shows the critical temperature for superconductivity ($T_c$) determined from $\rho_{ab}$ as a function of the percent concentration of the tetragonal FeSe phase.

## III. RESULTS AND DISCUSSION

In Fig. 2 (main panel) we show the temperature dependence of the in-plane resistivity $\rho_{ab}$ for five crystals No. 1, 2, 3, 4, and 6 grown in different crucibles. Their zero-field temperature region of the transition defined by the 10% and 90% points of the transition equals 9.9–12.7 K, 8.65–12 K, 8.9–12.3 K, 8–11.2 K, and 9.6–11.7 K. The inset (a) shows the enlarged resistivity near $T_c$ in order to emphasize the low-temperature behavior, and the inset (b) plots the values of $T_c$ (midpoint) determined from $\rho_{ab}$ as a function of the percent concentration of the tetragonal FeSe phase in the sample. We note that the upper points of the superconducting transition in the

TABLE I. Summary of the properties of the investigated crystals determined as described in the text: The sample number (No.), tetragonal phase percent, critical temperature ($T_c$), slope $(dH^*_{c2\|c}/dT)_{T_c'}$, slope $(dH^*_{c2\|ab}/dT)_{T_c'}$, upper critical fields $H^*_{c2\|c}(0)$ and $H^*_{c2\|ab}(0)$, coherence lengths at zero temperature $\xi_{ab}$ and $\xi_c$ obtained from the $\rho_n$ and $0.9\rho_n$ criteria.

| No. | tetr. ph. % | $T_c^{\text{midpoint}}$ (K) | $(dH^*_{c2\|c}/dT)_{T_c'}$ (T/K) | $(dH^*_{c2\|ab}/dT)_{T_c'}$ (T/K) | $H^*_{c2\|c}(0)^{0.9\rho_n}$ (T) | $H^*_{c2\|ab}(0)^{0.9\rho_n}$ (T) | $\xi_{ab}(0)^{0.9\rho_n}$ Å | $\xi_c(0)^{0.9\rho_n}$ Å |
|---|---|---|---|---|---|---|---|---|
| 1 | 100 | 11 | | $-6.1^{\rho_n}; -5.4^{0.9\rho_n}$ | | $\simeq$36 | | |
| 2 | 85 | 9.9 | $-3.9^{\rho_n}; -3.65^{0.9\rho_n}$ | $-5.9^{\rho_n}; -5^{0.9\rho_n}$ | 29 | $\simeq$34 | 33 | $\simeq$28.5 |
| 3 | 92 | 10.2 | | | 30 | | 32.5 | |
| 4 | 87 | 9.5 | | | 28 | $\simeq$31 | 34 | $\simeq$30 |
| 6 | 94 | 10.4 | $-4.5^{\rho_n}; -3.5^{0.9\rho_n}$ | | $\simeq$31 | | $\simeq$32 | |

magnetization curves were close to the temperatures of the superconducting transition determined from the cross point of two extrapolated lines drawn for the resistivity data around $T_c$.[12]

One can see that our crystals have the typical temperature dependencies of the in-plane $\rho_{ab}$ resistivity for FeSe crystals, and the values of the residual resistivity $\rho_{ab}(0)$ in crystals determined by linearly extrapolating the curves to zero temperature are comparable with the lowest value previously reported for FeSe (see, e.g., Refs. 13–15). The in-plane resistivity of the crystals shows an almost linear temperature dependence at temperatures $T < 200$ K, and the slope $\Delta\rho_{ab}/\Delta T$ lies between 0.6 and 1.3 $\mu\Omega$cm/K. The curves $\rho_{ab}(T)$ have a characteristic feature at $T \sim 80$ K related to the tetragonal-to-orthorhombic phase transition (marked by arrow) which has been observed previously in FeSe.[1,5,15] As may be seen from Fig. 2 [main panel and the inset (b)] and Table I, the slope $\Delta\rho_{ab}/\Delta T$ and the magnitude of $T_c$ increase with increasing tetragonal phase concentration.

Figure 3 shows the zero-field $\rho_{ab}$ and $\rho_c$ as a function of the temperature for two samples No. 1 and No. 2. The $\rho_c$ data are divided by 3 and 4. As for the case of $\rho_{ab}(T)$, the resistivity $\rho_c$ curves give an almost linear "metallic" temperature dependence. A parameter often used to characterize the interlayer coupling is the anisotropy of the resistivity

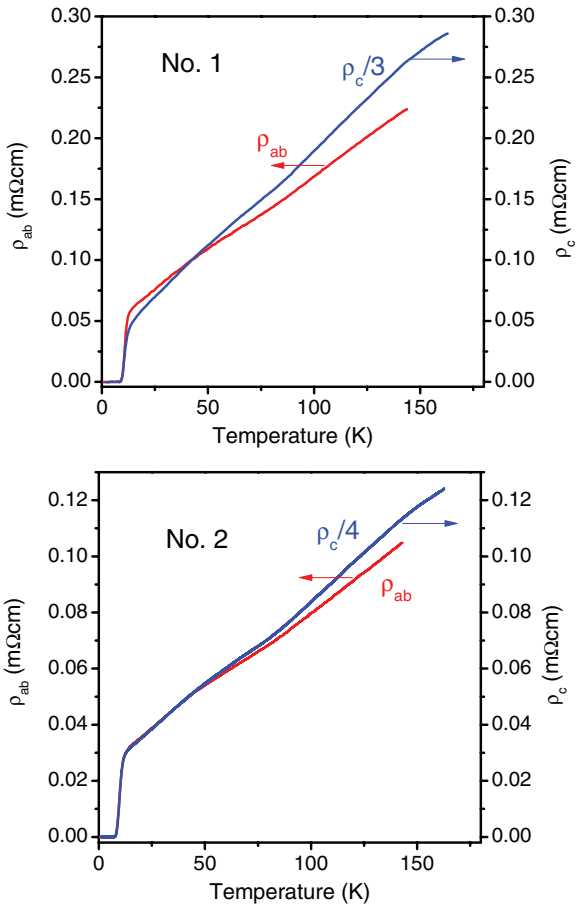


FIG. 3. (Color online) The zero-field $\rho_{ab}$ and $\rho_c$ as a function of the temperature for two samples No. 1 and No. 2. The $\rho_c$ data are divided by 3 and 4.

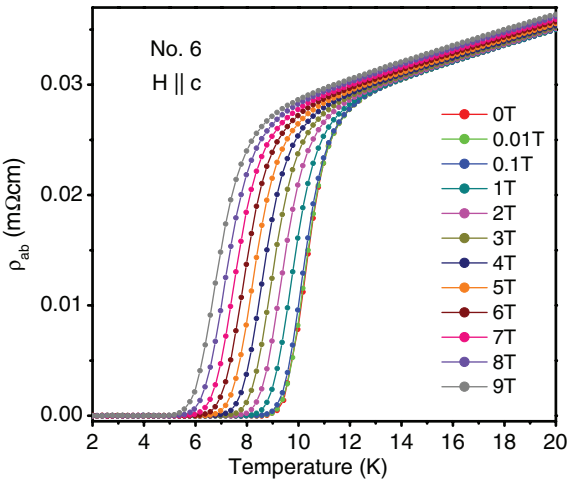


FIG. 4. (Color online) Temperature dependence of the in-plane $\rho_{ab}$ resistivity for crystal No. 6 with $T_c$ (midpoint) = 10.3 K for applied magnetic fields up to 9 T with direction perpendicular to the $ab$ plane of the crystal.

$\rho_c/\rho_{ab}$. The largest anisotropy ratio found here is $\rho_c/\rho_{ab} = 4$ just above $T_c$, indicating that the FeSe system is nearly three dimensional. We find that the anisotropy ratio in the zero-magnetic field is practically temperature independent for all samples. Such a behavior of the anisotropy ratio suggests that in-plane and out-of-plane transport in FeSe share the same scattering mechanism.

In Fig. 4 we report the temperature dependencies of the in-plane $\rho_{ab}$ resistivity for crystal No. 6 with $T_c$ (midpoint) = 10.4 K for applied magnetic fields up to 9 T with direction perpendicular to the $ab$ plane of the crystal. As is clear from Fig. 4, with increasing magnetic fields, the onset of superconductivity shifts to lower temperatures gradually. However, the resistive superconducting transitions do not show any field-induced broadening. Hence, it can be concluded that in the **H**‖**c** geometry the vortex-liquid state region is very narrow or even absent in FeSe. This is similar to FeTeSe system.[16]

The magnetic field dependence of resistivity $\rho_{ab}(H)$ of the sample No. 2 at various temperatures with the field direction perpendicular (a) and parallel (b) to the $ab$ plane of the crystal is presented in Fig. 5. At low temperature, the curves $\rho_{ab}(H)$ are almost parallel with respect to each other in the transition region. When the temperature is close but below $T_c$, the superconducting transition broadens. With increasing magnetic fields, the onset of superconductivity shifts to lower temperatures gradually for both magnetic field directions, but the resistive transition becomes considerably wider in the **H**‖**ab** geometry as compared with those in the **H**‖**c** configuration. Such behavior of the resistive transition in the **H**‖**ab** geometry can be explained by the vortex-liquid state similar to cuprates. It should be noted that at the determination of the temperature dependence of the resistive upper critical field in the case of a broadened superconducting transition different criteria can lead to a different temperature dependence for $H^*_{c2}(T)$.[17] Therefore, we determined the temperature dependence for the resistive upper critical field $H^*_{c2}$ by two different means.

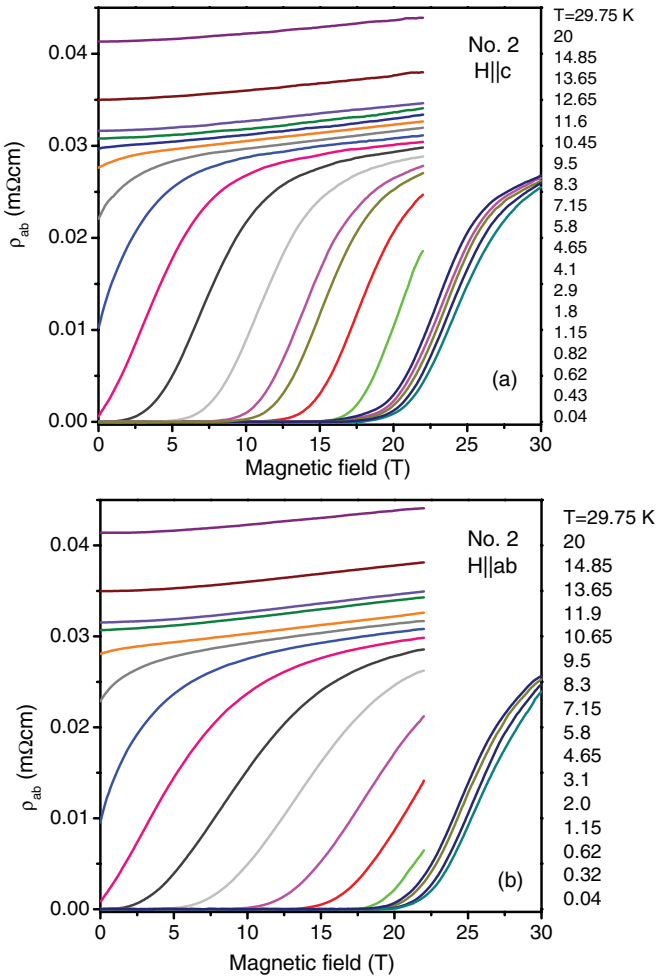


FIG. 5. (Color online) Resistive transitions of crystal No. 2 in magnetic field **H**‖**c** (a) and **H**‖**ab** (b) at different temperatures.

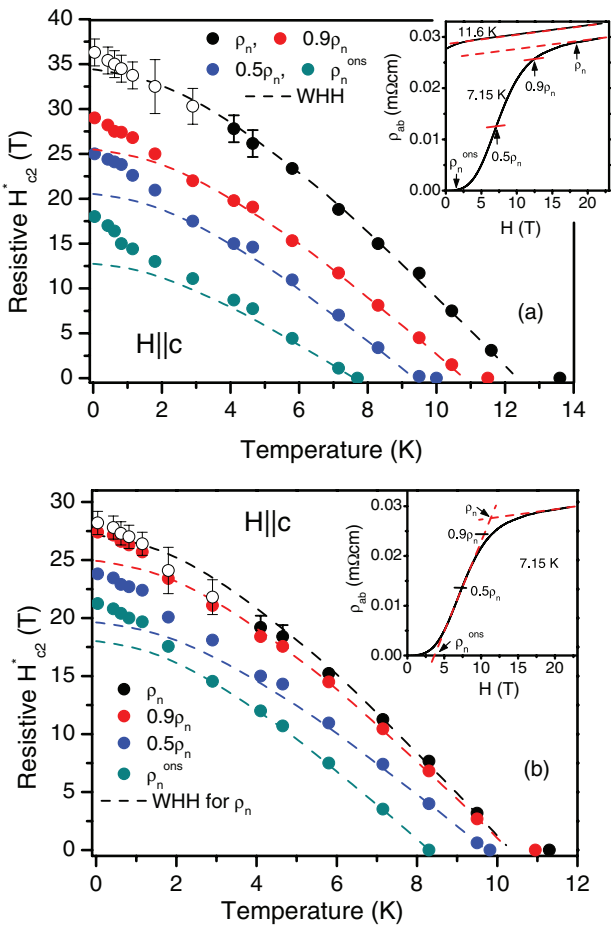


FIG. 6. (Color online) Temperature dependence of $H^*_{c2}$ for sample No. 2 extracted from the MR curves in Fig. 5(a) measured in the **H**‖**c** geometry together with the theoretical WHH curves. The "data points" shown by open circles were obtained from Fig. 5(a) by a linear extrapolation of $\rho_{ab}(H)$ to $\rho_{ab}(T) = \rho_n$. The red dashed lines and the arrows in the insets show the methods used to define $H^*_{c2}$ from the measured $\rho_{ab}(H)$ curves (see the text).

Figure 6(a) shows the temperature dependence of $H^*_{c2}$ for the sample No. 2 extracted from the magnetoresistance (MR) curves in Fig. 5(a) measured in the **H**‖**c** geometry together with the theoretical Werthamer, Helfand, and Hohenberg (WHH)[18] curves which describes the behavior of the upper critical field in conventional type-II superconductors without spin paramagnetic and spin-orbit effects. As can be seen from the inset to Fig. 6(a), the $H^*_{c2}$ values were obtained from the fields at which the resistivity of the samples has reached 100% ($\rho_n$), 90% ($0.9\rho_n$), and 50% ($0.5\rho_n$) of its normal-state values at a given temperature.

The "data points" shown by open circles were obtained from Fig. 5 by a linear extrapolation of $\rho_{ab}(H)$ to $\rho_{ab}(T) = \rho_n$ as it has been done previously in, e.g., Refs. 8 and 16. These points are displayed in order to show roughly a general trend for $H_{c2}(T)$ (the magnetoresistance in the normal state was taken into account). The onset $\rho_n^{\rm ons}$ was determined at zero resistivity, the field values corresponding approximately to the onset of flux flow (method 1).

Figure 6(b) also shows the temperature dependence of $H^*_{c2}$ for the sample No. 2 extracted from the MR curves in Fig. 5(a) together with the WHH curves but with the 100% ($\rho_n$), 90% ($0.9\rho_n$), 50% ($0.5\rho_n$), and $\rho_n^{\rm ons}$ determined from the intersection of two extrapolated lines; one is drawn through the MR curve in the normal state at the higher field and the other is drawn through the steepest part of the MR curve in the superconducting state (method 2). This is shown in the inset to Fig. 6(b).

Before addressing the $H^*_{c2}(T)$ data, it is of interest to present the temperature dependence of the in-plane resistivity of the sample at low temperatures for the magnetic field perpendicular to the *ab* plane. Figure 7 shows a semilogarithmic plot of $\rho_{ab}(T)$ at different fixed magnetic fields **H**‖**c** for the sample No. 2 extracted from the curves in Fig. 5(a) in order to emphasize the low-temperature behavior. The transition temperature of superconductivity is suppressed gradually and at low temperatures, the transition is broadened with increasing magnetic field. In spite of the strong broadening of the magnetic transitions one can see in Fig. 7 that the 30 T data at $T \leqslant 1$ K are almost temperature independent. Thus, we can be certain that the determination of the $H^*_{c2}$ values using the 90% criterion at these temperatures is well founded.

Returning to the determination of the temperature dependence of the resistive upper critical field in Fig. 6, one can see that for both methods the determination of $H^*_{c2}$

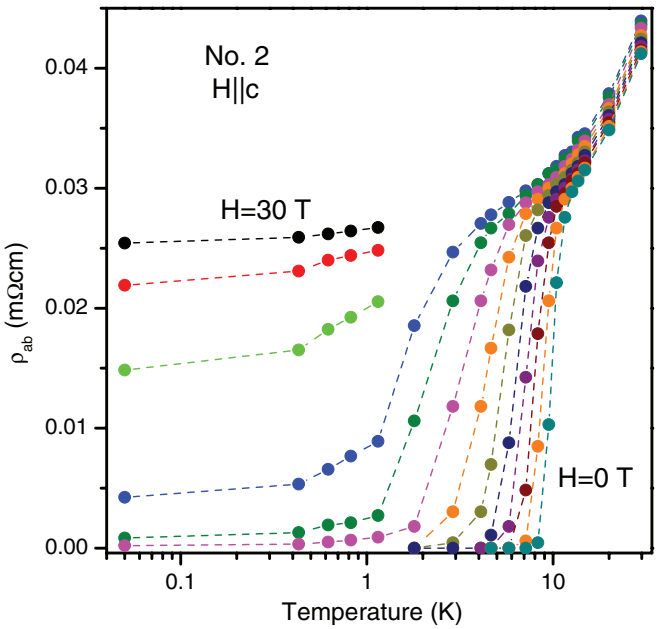


FIG. 7. (Color online) Semilogarithmic plot of $\rho_{ab}(T)$ at different fixed magnetic fields $\mathbf{H}\|\mathbf{c}$ for sample No. 2 extracted from the curves in Fig. 5(a). Between 0 and 30 T, the applied magnetic field was increased in steps of 2.5 T.

lead to similar conclusions; the experimental data obtained from the $\rho_n$ criterion down to $T/T_c \simeq 0.3$ can be entirely described by the conventional WHH theory. The temperature dependencies of $H^*_{c2}$ in Fig. 6 obtained from the $0.9\rho_n$, $0.5\rho_n$, and $\rho_n^{\text{ons}}$ criteria exhibit an upward curvature at $T \leqslant 2$ K. Analogous results were obtained on the sample No. 6. From the linear part of the $H^*_{c2}(T)$ dependence near $T_c$ as determined from the $\rho_n$ criterion, we obtained the slopes $dH^*_{c2}/dT_c = -1.55$ T/K and $-2.4$ T/K for the samples No. 2 and No. 6, respectively. It should be recognized that the strong broadening of the superconducting transition when the temperature is close to $T_c$ leads to a different temperature dependence of $H^*_{c2}$ versus $T$. Using a WHH-type extrapolation to lower temperature with $H^*_{c2}(0) = 0.693(-dH^*_{c2}/dT)_{T_c'}T_c'$ we obtained $H^*_{c2\|c}(0) \simeq 34$ T (sample No. 2) and 37 T (sample No. 6). Taking into account the experimental error, these values are close to the estimated $H^*_{c2\|c}(0)$ in our experiments from the $\rho_n$ criterion. Here, the $(dH^*_{c2}/dT)_{T_c'} = -3.9$ T/K (sample No. 2) and $-4.5$ T/K (sample No. 6) are taken to be the tangent of $H^*_{c2}(T)$ at temperatures close to $T_c$ and $T_c'$ the intersection of this tangent with the temperature axis. In case of the $0.9\rho_n$ criterion, we found $H^*_{c2\|c}(0) = 27.5$ T and 30 T for samples No. 2 and No. 6, respectively. These values are also close to the $H^*_{c2\|c}(0)$ found in our experiments.

In order to compare the temperature dependence of the $H^*_{c2}$ for different samples, in Fig. 8 we display the reduced critical field $h_{c2} = H^*_{c2}/(-dH^*_{c2}/dT)_{T_c}T_c$ as a function of the reduced temperature $T/T_c$ for two investigated samples No. 2 and No. 6 at field orientation $\mathbf{H}\|\mathbf{c}$ together with the theoretical WHH curve. The $H^*_{c2}$ values are the fields at which the resistivity of the samples has reached 100% and 90% of its normal-state values $\rho_n$ and obtained by two methods determination of $H^*_{c2}$ (see the insets to Fig. 6). The results

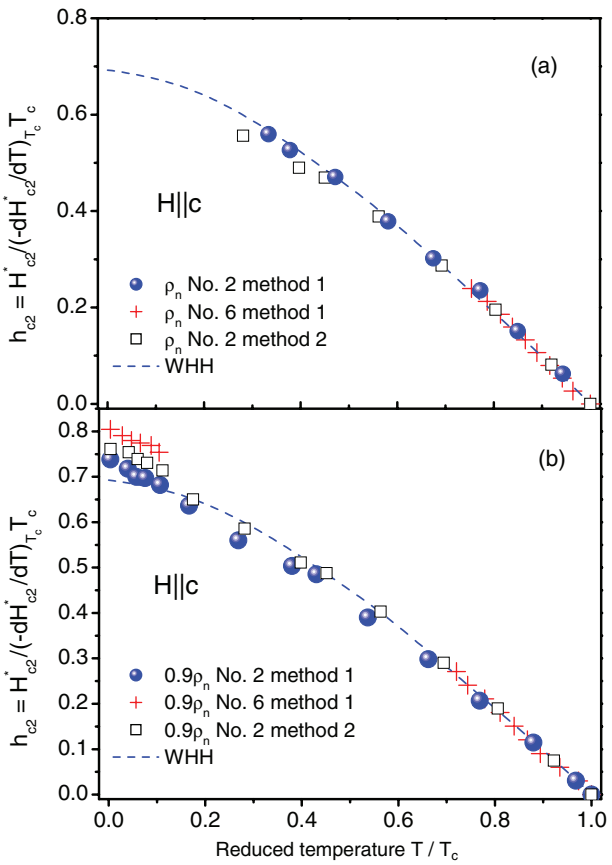


FIG. 8. (Color online) Reduced critical field $h_{c2} = H^*_{c2}/(-dH^*_{c2}/dT)_{T_c}T_c$ as a function of the reduced temperature $T/T_c$ for two samples No. 2 and No. 6 at field orientation $\mathbf{H}\|\mathbf{c}$ together with the theoretical WHH curve (dashed lines). The $H^*_{c2}$ values are the fields at which the resistivity of the samples has reached 100% (a) and 90% (b) of its normal-state values $\rho_n$ and obtained by two methods determination of $H^*_{c2}$ (see the insets to Fig. 6).

in Fig. 8 clearly shows that the data for the temperature dependence of the reduced critical field $h_{c2}$ can also be described by the conventional WHH theory down to $T/T_c \simeq 0.3$ for the 100% criterion (in available fields for us) and except for the small region at lower temperatures $T/T_c < 0.1$ for the 90% criterion. In other words, down to this temperature in the $\mathbf{H}\|\mathbf{c}$ configuration, we did not observe any unusual behavior of the resistive upper critical field $H^*_{c2}$ in our FeSe single crystals. By this we mean that the upper critical field $H^*_{c2\|c}$ obtained from the $0.9\rho_n$ criterion for our FeSe single crystals in $\mathbf{H}\|\mathbf{c}$ configuration approximately equals 29 T and 31 T for samples No. 2 and No. 6, respectively. In regard to the upward curvature of the temperature dependencies of $H^*_{c2}$ at $T \leqslant 2$ K in Fig. 6 obtained from the $0.9\rho_n$, $0.5\rho_n$, and $\rho_n^{\text{ons}}$ criteria, Hunte *et al.*[9] have interpreted the observed upward curvature of $H_{c2}(T)$ in LaFeAsOF as a signature of multiband superconductivity in this family of compounds, which could lead to a significant raise of $H_{c2}(T = 0)$ with respect to the WHH extrapolation. We also measured MR for the samples No. 3 and 4 over a temperature range 0.05–1.15 K and found that $H^*_{c2\|c}(0) \simeq 30$ T and 28 T, respectively (for 90% criterion).

Figure 9 shows the temperature dependence of $H^*_{c2}$ for sample No. 2 determined by the two methods applied in

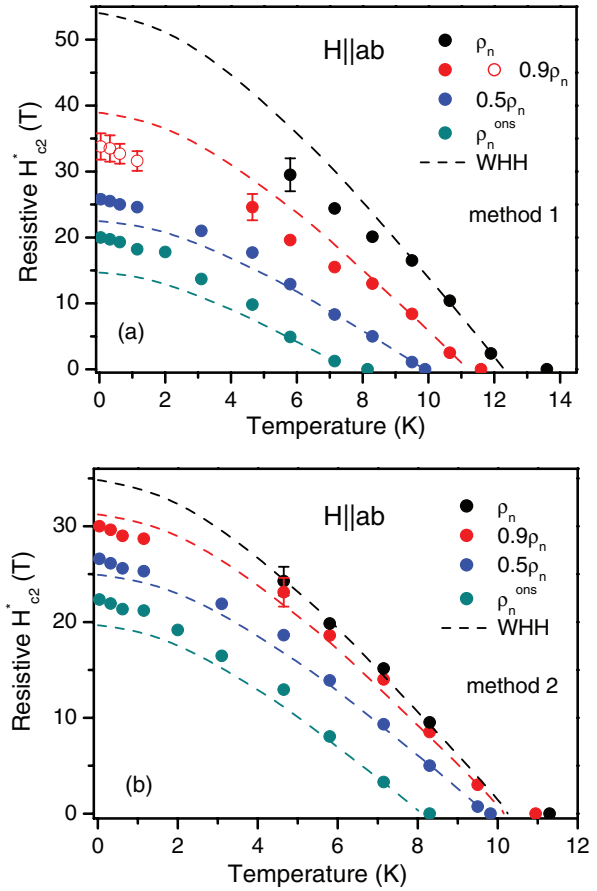


FIG. 9. (Color online) Temperature dependence of $H^*_{c2}$ for sample No. 2 extracted from the MR curves in Fig. 5(b) measured in the **H**‖**ab** geometry together with the theoretical WHH curves (dashed lines). The "data points" shown by open circles were obtained from Fig. 5(b) by a linear extrapolation of $\rho_{ab}(H)$ to $\rho_{ab}(T) = \rho_n$.

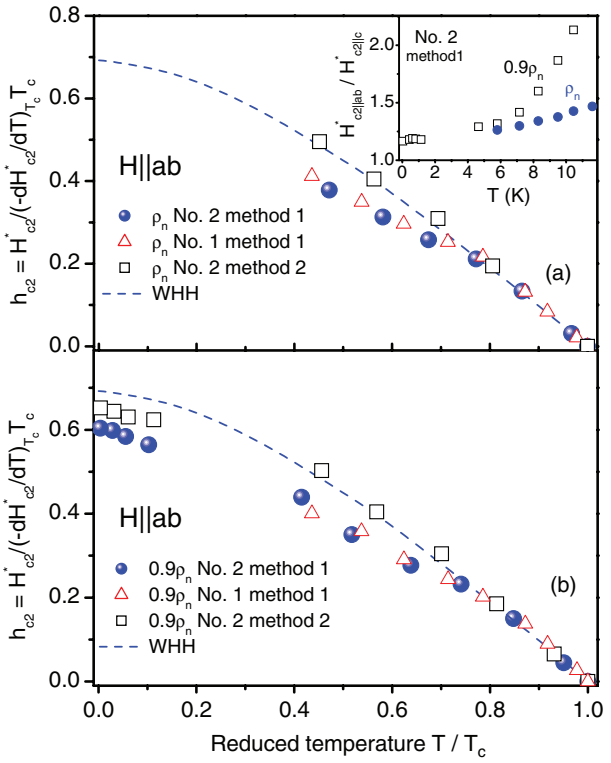


FIG. 10. (Color online) Reduced critical field $h_{c2} = H^*_{c2}/(-dH^*_{c2}/dT)_{T_c}T_c$ as a function of the reduced temperature $T/T_c$ for samples No. 1 and No. 2 at field orientation **H**‖**ab** together with the theoretical WHH curve. The $H^*_{c2}$ values are the fields at which the resistivity of the samples has reached 100% (a) and 90% (b) of its normal-state values $\rho_n$ and obtained by two methods determination of $H^*_{c2}$ (see the insets to Fig. 6). The inset in (a) shows the temperature dependence of the anisotropy parameter $\gamma = H^*_{c2\|ab}/H^*_{c2\|c}$ for the sample No. 2, obtained from the 100% and 90% criteria by the method 1.

Figs. 6(a) and 6(b) but extracted from the MR curves in Fig. 5(b) measured in the **H**‖**ab** geometry together with the theoretical WHH curves (dashed lines). As is seen from Fig. 9, the data for the **H**‖**ab** geometry obtained by the method 1, depart strongly from the WHH curves. One must note that in this case, the broadening of the superconducting transition and the rounding of the top of the transition make it impossible to define the value of the upper critical field exactly. Because of this, the departure already depends on the method and criterion chosen for the determination of $H^*_{c2}$. Nevertheless, there are strong reasons to believe that the $H^*_{c2}$ obtained from the $\rho_n$ and $0.9\rho_n$ criteria and determined by the method 1 most closely correspond to true values of the resistive upper critical field.[19] Similar results were obtained on the sample No. 1, however, because of the very large values of the upper critical fields of sample No. 1 in the **H**‖**ab** geometry, we could determine the $H^*_{c2}$ values down to $T/T_c < 0.2$ only. In the **H**‖**ab** configuration, the WHH formula predicts the value $H^*_{c2\|ab}(0) = 54$ T with $(dH^*_{c2}/dT)_{T_c} = -5.9$ T/K and 55.5 T with $(dH^*_{c2}/dT)_{T_c} = -6.1$ T/K for the samples No. 2 and No. 1, respectively, obtained from the 100% criterion. The upper critical field in the **H**‖**ab** geometry from high-magnetic field measurement is much smaller than that predicted using the WHH model.

In Fig. 10 (main panel) we display the reduced critical field $h_{c2} = H^*_{c2}/(-dH^*_{c2}/dT)_{T_c}T_c$ as a function of the reduced temperature $T/T_c$ for the samples No. 1 and No. 2 at field orientation **H**‖**ab** together with the theoretical WHH curve. The $H^*_{c2}$ values are the fields at which the resistivity of the samples has reached 100% (a) and 90% (b) of its normal-state values $\rho_n$ and obtained by two methods determination of $H^*_{c2}$ (see the insets to Fig. 6). By this means the upper critical field $H^*_{c2\|ab}$ obtained from the $0.9\rho_n$ criterion for samples No. 1 and No. 2 approximately equals 36 T and 34 T, respectively. We also measured $H^*_{c2\|ab}(T)$ for the sample No. 4 over a temperature range 0.05–1.15 K and found that $H^*_{c2\|ab}(0) \simeq 31$ T from the $0.9\rho_n$ criterion.

The large deviation from the conventional WHH theory in case of $H^*_{c2\|ab}$ geometry in Figs. 9(a) and 10(a) for the data obtained by method 1 can most likely be explained by a spin-paramagnetic limitation.[19] Using the energy gap value $\Delta_0 = 2.2$ meV, determined from specific heat measurements,[20] we can estimate the Clogston paramagnetic limit[21] $H_p(0) = \Delta_o/\mu_B\sqrt{2} \simeq 15$ T ($\mu_B$ is Bohr magneton). If we take the experimental values of $T_c = 12$ K for sample No. 2 obtained from the 90% criterion, we can also obtain an estimate of the paramagnetic field by using the other Clogston

formula $H_p(0) = 1.84T_c$, which gives $H_p(0) \simeq 22$ T (under the assumption that $2\Delta_0 = 3.5k_BT_c$). Both these values are smaller than the experimental values of $H^*_{c2\|c}(0)$ and $H^*_{c2\|ab}(0)$. A similar suppression of the paramagnetic effect was also observed in the conventional layered superconductors $NbSe_2$ and $TaS_2$. Owing to the uncertainty of the paramagnetic limit given by the simple Clogston formulas, we have previously derived an expression for $H_p(0)$ for the paramagnetic limitation of superconductivity for the field parallel to the layers based on a Ginzburg-Landau calculation.[22] Using the equation (8) in Ref. 22 and taking $T_c = 12$ K for the sample No. 2 in 90% point of the transition, one can obtain the estimate $H_p(0) \simeq 76/g$ T. If one takes the free electron $g$-factor value $g = 2$, we find $H_p(0) \simeq 38$ T which is reasonably close to the measured value of $H^*_{c2\|ab}(0)$ in 90% criterion (see Table I).

We can also estimate the $ab$-plane and $c$-axis coherence lengths at zero temperature from the anisotropic Ginsburg-Landau relations $H^*_{c2\|c} = \Phi_0/2\pi\xi^2_{ab}$ and $H^*_{c2\|ab} = \Phi_0/2\pi\xi_{ab}\xi_c$. Using the data from the $\rho = 0.9\rho_n$ criterion we get for four samples (No. 2, 3, 4, and 6) $\xi_{ab} \simeq 32 - 34$ Å in the $ab$ plane and $\xi_c \simeq 28.5 - 30$ Å in the $c$ direction. We find that an anisotropy parameter $\gamma = H^*_{c2\|ab}/H^*_{c2\|c} = \xi_{ab}/\xi_c$ equals 1.17 and 1.12 for the samples No. 2 and No. 4, respectively. As in all Fe-based superconductors, this parameter is unusually low compared to that of high $T_c$ cuprate superconductors (see, e.g., Ref. 23, and references cited therein). Although in the case of one-layer cuprate Bi-2201 single crystals $\gamma = 1.9$.[22]

It is significant that the anisotropy parameter $\gamma$ in our FeSe crystals decreases with decreasing temperature and FeSe becomes nearly isotropic when the temperature $T \to 0$. This is evident from the inset to Fig. 10 where we display the temperature dependence of the anisotropy parameter $\gamma = H^*_{c2\|ab}/H^*_{c2\|c}$ for the sample No. 2 obtained from the 100% and 90% criteria by the method 1. It is interesting to note that the values and the temperature dependence of $\gamma$ are very close to those obtained from resistivity measurements for FeSeTe in Refs. 16 and 24. In all probability, such unusual temperature dependence of the anisotropy parameter $\gamma$ is indicative of multiband superconductivity in FeSe as in the case of PrFeAsO[25] and in two-band anisotropic superconductor $MgB_2$.[26] Anomalous behavior of $\gamma$ was also argued in Ref. 27.

For conventional layered superconductors, the anisotropy parameter is usually expressed by the ratio $\gamma = \sqrt{m^*_c/m^*_{ab}}$ between the effective masses of the quasiparticles along the $c$ axis and the $ab$ plane, which can be related to the transport anisotropy with $\gamma \simeq \sqrt{\rho_c/\rho_{ab}}$ and the upper critical field anisotropy $\gamma = H^*_{c2\|ab}/H^*_{c2\|c}$.[28] As can be seen from Fig. 3, the resistivity anisotropy of the sample No. 2 near $T_c$ equals 4 and then $\gamma \simeq \sqrt{\rho_c/\rho_{ab}} = H^*_{c2\|ab}/H^*_{c2\|c} = 2$. That is close to the measured value of $\gamma$ at $T = T_c$ (inset to Fig. 10).

## IV. CONCLUSION

We have studied the resistive superconducting transition in FeSe single crystals down to $T = 40$ mK in continuous magnetic fields up to 30 T applied perpendicular and parallel to the $ab$ plane. In the $\mathbf{H}\|\mathbf{c}$ geometry the temperature dependence of the resistive upper critical field $H^*_{c2}$, determined as the field at which the in-plane resistivity in the transition region is 90% of the normal state resistivity, is down to temperatures $T/T_c < 0.006$ is in close agreement with the Werthamer-Helfand-Hohenberg theoretical curve which describes the behavior of the upper critical field in conventional type-II superconductors without spin paramagnetic and spin-orbit effects. In contrast, for the $\mathbf{H}\|\mathbf{ab}$ geometry, the data depart from the WHH model with increasing applied magnetic field according to the paramagnetic limitation of superconductivity. The anisotropy parameter $\gamma$ in our FeSe crystals decreases with decreasing temperature and FeSe becomes nearly isotropic when the temperature $T \to 0$.

## ACKNOWLEDGMENTS

We thank V. V. Rodin and S. G. Chernook for the careful x-ray and composition studies of the single crystals. The work at LNCMI was partially supported by EUROMAGNET II under the SP7 transnational access program of the European Union under Contract No. 228043.

[1] F. C. Hsu, J. Y. Luo, K. W. Yeh, T. K. Chen, T. W. Huang, P. M. Wu, Y. C. Lee, Y. L. Huang, Y. Y. Chu, D. C. Yan, and M. K. Wu, Proc. Natl. Acad. Sci. USA **105**, 14262 (2008).

[2] Y. Mizuguchi, F. Tomioka, S. Tsuda, T. Yamaguchi, and Y. Takano, Appl. Phys. Lett. **93**, 152505 (2008).

[3] S. Medvedev, T. M. McQueen, I. A. Troyan, T. Palasyuk, M. I. Eremets, R. J. Cava, S. Naghavi, F. Casper, V. Ksenofontov, G. Wortmann, and C. Felser, Nat. Mater. **8**, 630 (2009).

[4] T. M. McQueen, Q. Huang, V. Ksenofontov, C. Felser, Q. Xu, H. Zandbergen, Y. S. Hor, J. Allred, A. J. Williams, D. Qu, J. Checkelsky, N. P. Ong, and R. J. Cava, Phys. Rev. B **79**, 014522 (2009).

[5] E. Pomjakushina, K. Conder, V. Pomjakushin, M. Bendele, and R. Khasanov, Phys. Rev. B **80**, 024517 (2009).

[6] T. Taen, Y. Tsuchiya, Y. Nakajima, and T. Tamegai, Phys. Rev. B **80**, 092502 (2009).

[7] B. Buchner and C. Hess, Nat. Mater. **8**, 615 (2009).

[8] G. Fuchs, S.-L. Drechsler, N. Kozlova, G. Behr, A. Köhler, J. Werner, K. Nenkov, R. Klingeler, J. Hamann-Borrero, C. Hess, A. Kondrat, M. Grobosch, A. Narduzzo, M. Knupfer, J. Freudenberger, B. Büchner, and L. Schultz, Phys. Rev. Lett. **101**, 237003 (2008).

[9] F. Hunte, J. Jaroszynski, A. Gurevich, D. C. Larbalestier, R. Jin, A. S. Sefat, M. A. McGuire, B. C. Sales, D. K. Christen, and D. Mandrus, Nature (London) **453**, 903 (2008).

[10] S. Haindl, M. Kidszun, A. Kauffmann, K. Nenkov, N. Kozlova, J. Freudenberger, T. Thersleff, J. Hänisch, J. Werner, E. Reich, L. Schultz, and B. Holzapfel, Phys. Rev. Lett. **104**, 077001 (2010).

[11] H. Lei, D. Graf, R. Hu, H. Ryu, E. S. Choi, S. W. Tozer, and C. Petrovic, Phys. Rev. B **85**, 094515 (2012).

[12] J. I. Gorina, G. A. Kaljuzhnaia, M. V. Golubkov, V. V. Rodin, N. N. Sentjurina, and S. G. Chernook, Crystallogr. Rep. **57**, 585 (2012).

[13]T. M. McQueen, A. J. Williams, P. W. Stephens, J. Tao, Y. Zhu, V. Ksenofontov, F. Casper, C. Felser, and R. J. Cava, Phys. Rev. Lett. **103**, 057002 (2009).
[14]J. Wen, G. Xu, G. Gu, J. M. Tranquada, and R. J. Birgeneau, Rep. Prog. Phys. **74**, 124503 (2011).
[15]M. de Souzaa, A.-A. Haghighirad, U. Tutsch, W. Assmus, and M. Lang, Eur. Phys. J. **77**, 101 (2010).
[16]H. C. Lei, R. W. Hu, E. S. Choi, J. B. Warren, and C. Petrovic, Phys. Rev. B **81**, 094518 (2010).
[17]D. J. C. Walker, O. Laborde, A. P. Mackenzie, S. R. Julian, A. Carrington, J. W. Loram, and J. R. Cooper, Phys. Rev. B **51**, 9375 (1995).
[18]N. R. Werthamer, E. Helfand, and P. C. Hohenberg, Phys. Rev. **147**, 295 (1966).
[19]S. I. Vedeneev, A. G. M. Jansen, E. Haanappel, and P. Wyder, Phys. Rev. B **60**, 12467 (1999).
[20]J. Y. Lin, Y. S. Hsieh, D. A. Chareev, A. N. Vasiliev, Y. Parsons, and H. D. Yang, Phys. Rev. B **84**, 220507 (2011).
[21]A. Clogston, Phys. Rev. Lett. **3**, 266 (1962).
[22]S. I. Vedeneev, C. Proust, V. P. Mineev, M. Nardone, and G. L. J. A. Rikken, Phys. Rev. B **73**, 014528 (2006).
[23]M. Bendele, S. Weyeneth, R. Puzniak, A. Maisuradze, E. Pomjakushina, K. Conder, V. Pomjakushin, H. Luetkens, S. Katrych, A. Wisniewski, R. Khasanov, and H. Keller, Phys. Rev. B **81**, 224520 (2010).
[24]M. H. Fang, J. H. Yang, F. F. Balakirev, Y. Kohama, J. Singleton, B. Qian, Z. Q. Mao, H. D. Wang, and H. Q. Yuan, Phys. Rev. B **81**, 020509 (2010).
[25]R. Okazaki, M. Konczykowski, C. J. van der Beek, T. Kato, K. Hashimoto, M. Shimozawa, H. Shishido, M. Yamashita, M. Ishikado, H. Kito, A. Iyo, H. Eisaki, S. Shamoto, T. Shibauchi, and Y. Matsuda, Phys. Rev. B **79**, 064520 (2009).
[26]V. G. Kogan, Phys. Rev. B **66**, 020509(R) (2002).
[27]J.-Y. Lin, Y. S. Hsieh, D. A. Chareev, A. N. Vasiliev, Y. Parsons, and H. D. Yang, Phys. Rev. B **84**, 220507(R) (2011).
[28]M. Tinkham, *Introduction to Superconductivity* (Krieger, Malabar, Florida, 1955).